



# Fast flash frozen synthesis of holey few-layer g-C<sub>3</sub>N<sub>4</sub> with high enhancement of photocatalytic reactive oxygen species evolution under visible light irradiation

Shifei Kang, Lu Zhang, Chaochuang Yin, Yaguang Li, Lifeng Cui\*, Yangang Wang\*

Department of Environmental Science and Engineering, University of Shanghai for Science and Technology, Shanghai 200093, China

## ARTICLE INFO

### Article history:

Received 5 January 2017

Received in revised form 22 February 2017

Accepted 19 April 2017

Available online 22 April 2017

### Keywords:

Graphitic carbon nitride

Reactive oxygen species

Few-layer

Flash frozen exfoliation

Environmental-friendly synthesis

## ABSTRACT

Few-layer graphitic carbon nitride (g-C<sub>3</sub>N<sub>4</sub>) nanosheets with holey porous structures were prepared by fast treatment bulk g-C<sub>3</sub>N<sub>4</sub> using environmental-friendly flash frozen exfoliation method within several seconds. The products were characterized by X-ray diffractometry, X-ray photoelectron spectroscopy, Fourier transform infrared spectroscopy, transmission electron microscopy and electrochemical impedance spectroscopy. The foam-like holey ultrathin g-C<sub>3</sub>N<sub>4</sub> nanosheets exhibit high crystallinity, narrower band gap (2.46 eV), more exposed edges and enhanced electron transport ability. N<sub>2</sub> adsorption-desorption tests show that the few-layer g-C<sub>3</sub>N<sub>4</sub> has a slightly-enlarged specific surface area of 135.6 m<sup>2</sup>/g and enriched small mesopores. Compared with bulk g-C<sub>3</sub>N<sub>4</sub>, the few-layer holey g-C<sub>3</sub>N<sub>4</sub> showed a significantly enhanced ability of reactive oxygen species generation and 4-fold higher activity for visible-light-driven Rhodamine B photodegradation, which were mainly attributed to the enriched active sites and shorter pathway from the carrier to the reaction sites. These findings provide an inspiration for clean scale-up production of highly-active few-layer g-C<sub>3</sub>N<sub>4</sub> photocatalysts towards environmental and biological applications.

© 2017 Elsevier B.V. All rights reserved.

## 1. Introduction

The increasing awareness of energy crisis and environmental pollution has stimulated intensive research on solar energy conversion in recent years [1]. At the same time, non-invasive phototherapy, referred to the removal of toxic metabolite or inactivate tumor cells *in vivo* after exposure to light with specific wavelengths, has also attracted wide attention [2]. Among all these applications, the core challenge is how to prepare an appropriate semiconductor photocatalyst to support a high-efficient energy utility system [3]. However, the practical effects of conventional metallic oxide semiconductors (e.g. TiO<sub>2</sub>) and metal sulfide semiconductors (e.g. CdS) are unsatisfactory due to their fairly low quantum efficiency or poor stability [4,5]. As a new generation of nonmetallic alternative semiconductors to traditional materials, layer-structured polymeric graphitic carbon nitride (g-C<sub>3</sub>N<sub>4</sub>) has many extraordinary features, such as environmental friendliness, reasonable cost, high stability, and excellent optical and electronic properties [6–8].

In this regard, g-C<sub>3</sub>N<sub>4</sub> has been widely studied for the applications in photocatalytic organic pollution degradation, water splitting and phototherapy under visible light irradiation [9–12].

However, the photocatalytic activity of bulk g-C<sub>3</sub>N<sub>4</sub> is usually limited by the low quantum efficiency and poor active sites [13,14]. Several modification proposals have been developed, such as nanostructure tailoring [15,16], doping with metal or nonmetal element [9,17], and g-C<sub>3</sub>N<sub>4</sub> based semiconductors heterojunctions constructing [18,19], among which the fabrication of few-layer g-C<sub>3</sub>N<sub>4</sub> was the ineluctable foundation [20,21]. Motivated by the two-dimensional (2D) crystal graphene that has many interesting physicochemical properties, researchers have made great efforts to prepare g-C<sub>3</sub>N<sub>4</sub> nanosheets with single-layer or few-layer thickness [22]. Different from bulk g-C<sub>3</sub>N<sub>4</sub> in which all the g-C<sub>3</sub>N<sub>4</sub> layers are densely-stacked, the few-layer g-C<sub>3</sub>N<sub>4</sub> nanosheets possess very internally-reactive surfaces as well as exotic optoelectronic properties which is favorable in utilization of visible light irradiation. Thus the ultrathin g-C<sub>3</sub>N<sub>4</sub> photocatalysts exfoliating from bulk g-C<sub>3</sub>N<sub>4</sub> has been widely employed in environmental, energetic and phototherapy applications [23]. Recently, Li et al. synthesized foam-like holey ultrathin g-C<sub>3</sub>N<sub>4</sub> nanosheets through long-time thermal treatment of bulk g-C<sub>3</sub>N<sub>4</sub>, this 2D in-plane holey ultrathin g-C<sub>3</sub>N<sub>4</sub> exhibit superior photocatalytic activity in dye remove and H<sub>2</sub> pro-

\* Corresponding authors.

E-mail addresses: lifeng.cui@gmail.com (L. Cui), ygwang8136@gmail.com (Y. Wang).

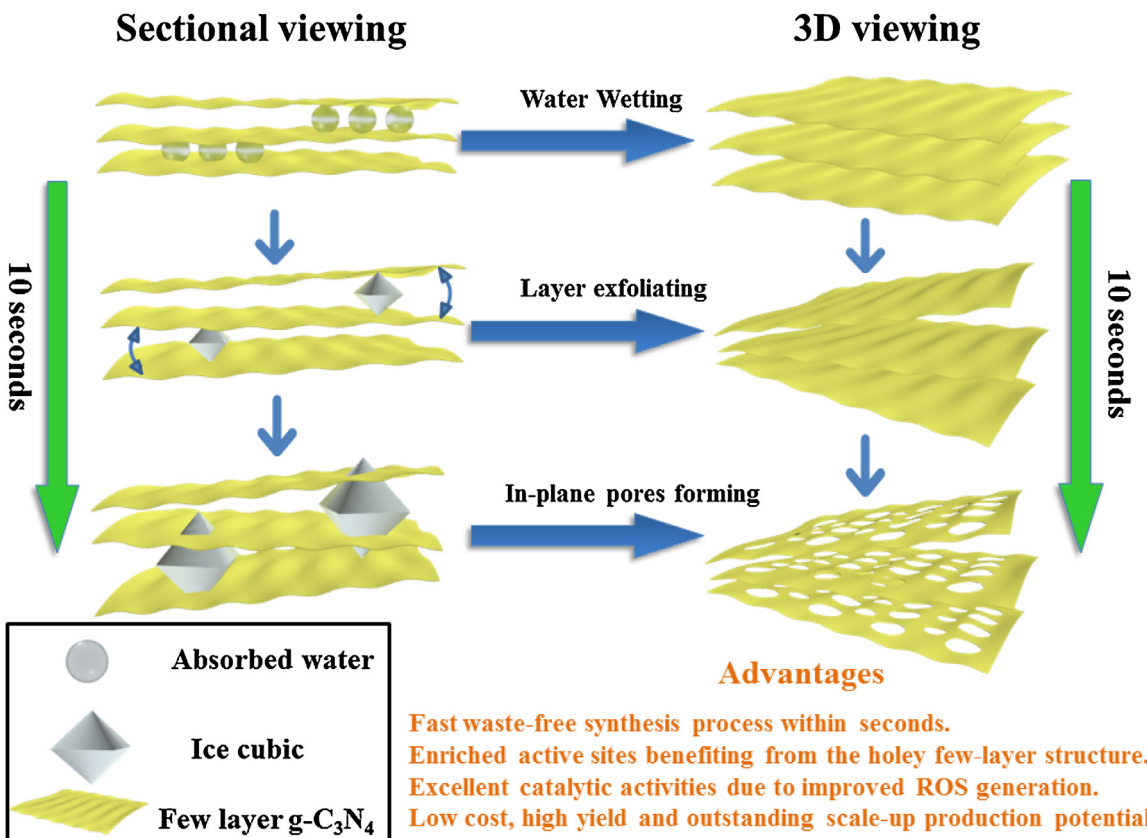


Fig. 1. Schematic illustration of flash frozen exfoliation process of few-layer  $\text{g-C}_3\text{N}_4$ .

duction under visible light [24]. In our previous work, hybrid few layer carbon/ $\text{g-C}_3\text{N}_4$  composites was prepared through a facile one-step pyrolysis method as high-performance catalysts for  $\text{CO}_2$  photoreduction. This ultrathin photocatalyst exhibit enlarged surface area and accelerated charge carrier separation rate, leading to an excellent  $\text{CO}$  and  $\text{CH}_4$  yield which were more than twice as high as that of bulk  $\text{g-C}_3\text{N}_4$ . Therefore, the few-layer  $\text{g-C}_3\text{N}_4$  nanosheets exfoliated by bulk  $\text{g-C}_3\text{N}_4$  as well as modification of polymeric melon units of  $\text{g-C}_3\text{N}_4$  has been proved to be an effective strategy to optimize the electronic structure and improve the photocatalytic performance of  $\text{g-C}_3\text{N}_4$  [25].

Unfortunately, as far as we know, most of the existing methods to fabricate few-layer  $\text{g-C}_3\text{N}_4$  (e.g. liquid-phase exfoliation, thermal etching, electrochemical and mechanical exfoliation) are usually low-yield, time-consuming and even cause further pollution due to the use of acid or surfactant [26–30]. In view of the fascinating properties of 2D in-plane holey ultrathin  $\text{g-C}_3\text{N}_4$ , the advanced process with environmental friendliness, high efficiency, free pollution and low energy consumption is still highly desirable.

Meanwhile, reactive oxygen species (ROS) plays a pivotal role in both photocatalytic organic pollution degradation and biomedical photodynamic therapy (PDT) applications. The ROS inspired by visible and near-infrared irradiations can not only oxidize environmental organic contaminants but also inactivate tumor cells efficiently. Recently, Zheng et al. reported the carbon-dot decorated  $\text{g-C}_3\text{N}_4$  nanosheets as photocatalyst for ROS generation *in vivo* against solid tumors. The unique and tunable physicochemical properties of few-layer  $\text{g-C}_3\text{N}_4$  advance the nontoxic materials as promising choice in solar energy conversion and cancer PDT [31]. Nevertheless, there is rare discussion on ROS generation and utility based on  $\text{g-C}_3\text{N}_4$  materials, and the ROS generation mechanism together with few-layer  $\text{g-C}_3\text{N}_4$  should be explored extensively.

Herein, we invented a fast flash frozen method to fabricate considerable few-layer  $\text{g-C}_3\text{N}_4$  nanosheets as a high-performance visible-light-driven photocatalyst. This waste-free approach eliminated the use of any traditional used acid and surfactant. In the simple fabrication process, a relatively small amount of liquid nitrogen was used as a flash freezing agent to treat wet bulk  $\text{g-C}_3\text{N}_4$  directly to achieve  $\text{g-C}_3\text{N}_4$  exfoliation for the first time. The physicochemical properties and photocatalytic performance of the obtained few-layer  $\text{g-C}_3\text{N}_4$  were investigated systematically. Also the unique ROS generation mechanism of this foam-like holey porous few-layer  $\text{g-C}_3\text{N}_4$  under visible light irradiation was discussed.

## 2. Experimental

### 2.1. Preparation of bulk $\text{g-C}_3\text{N}_4$

The bulk  $\text{g-C}_3\text{N}_4$  was prepared using a previous reported method of directly heating urea [32]. Specifically, 5 g of urea in a crucible with a cover was heated at 550 °C for 4 h and the heating rate of this condensation reaction was 5 °C/min. The whole preparation process was carried out in static air without any protection of inert gas. After natural cooling, the yellow final products were collected and grinded into fine powder for further use.

### 2.2. Preparation of few-layer $\text{g-C}_3\text{N}_4$

The few-layer  $\text{g-C}_3\text{N}_4$  was prepared by fast flash freezing exfoliation of bulk  $\text{g-C}_3\text{N}_4$  in liquid nitrogen. In detail, the wet bulk  $\text{g-C}_3\text{N}_4$  was synthesized by stirring the mixture of bulk  $\text{g-C}_3\text{N}_4$  and water for 1 h, the weight ratio of  $\text{g-C}_3\text{N}_4$  and water was chosen as 1:1 to permit a smoothly stirring and fully wetting. Subsequently,

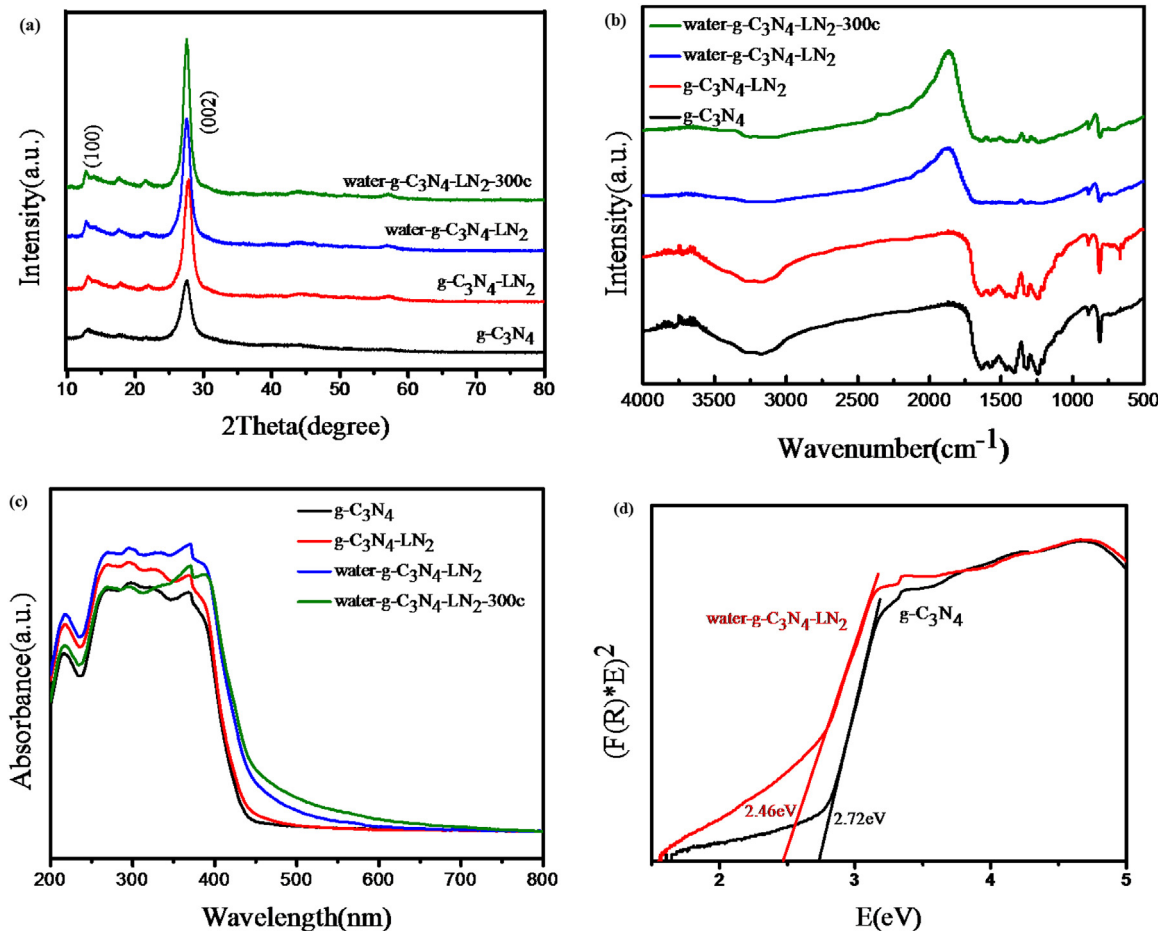


**Fig. 2.** (a) XRD patterns (b) FT-IR spectra and (c) UV-vis absorption spectra of different photocatalysts. (d) Estimated band gaps of the bulk g-C<sub>3</sub>N<sub>4</sub> and water-g-C<sub>3</sub>N<sub>4</sub>-LN<sub>2</sub>.

the dry bulk g-C<sub>3</sub>N<sub>4</sub> and wet bulk g-C<sub>3</sub>N<sub>4</sub> were dispersed in adequate liquid nitrogen for 10 s to guarantee the full freezing. Then the g-C<sub>3</sub>N<sub>4</sub> ice cubes were heated to melt and vacuum-dried at room temperature. The raw g-C<sub>3</sub>N<sub>4</sub>, liquid-nitrogen-treated dry g-C<sub>3</sub>N<sub>4</sub> and liquid-nitrogen-treated wet g-C<sub>3</sub>N<sub>4</sub> were designated as g-C<sub>3</sub>N<sub>4</sub>, g-C<sub>3</sub>N<sub>4</sub>-LN<sub>2</sub> and water-g-C<sub>3</sub>N<sub>4</sub>-LN<sub>2</sub>, respectively. To investigate the thermal stability of water-g-C<sub>3</sub>N<sub>4</sub>-LN<sub>2</sub>, we further heated it to 300 °C for 4 h and denoted as water-g-C<sub>3</sub>N<sub>4</sub>-LN<sub>2</sub>-300c.

### 2.3. Characterization

X-ray diffraction (XRD) patterns were identified by a Bruker Advanced D8 diffractometer (Germany) with Cu-K $\alpha$  radiation, operated at 40 kV and 40 mA (scanning step: 0.02°/s) in the 2 $\theta$  range of 10–80°. The Fourier transform infrared spectra (FT-IR) of the samples were recorded using a Nicolet Nexus 470 spectrometer. X-ray photoelectron spectroscopy (XPS) analysis was carried on Thermo ESCALAB 250 XPS instrument with Al K $\alpha$  monochromatization. Transmission electron microscopy (TEM) images were obtained with JEM-2100F microscope with an accelerating voltage of 200 kV. The nitrogen adsorption-desorption isotherms the samples was measured on Micromeritics Tristar 3000 analyzer at 77.4 K. UV-vis diffuse reflectance spectra (UV-vis DRS) were performed by using Cary 500 spectrometer. The electrochemical impedance spectroscopy (EIS) was recorded by a Chi660e electrochemical workstation based on a conventional three-electrode system with a frequency range from 0.01 Hz to 100 kHz at the circuit potential.

### 2.4. Photocatalytic ROS generation activity measurement

The photocatalytic oxidation activity of each sample was preliminary examined by monitoring the degradation of an aqueous suspension of Rhodamine B (RhB) (10 mg/L, 50 mL) in a quartz tube with the presence of 20 mg catalyst under visible light irradiation (500 W Xe lamp light source with a 420 nm optical filter), the light intensity on quartz tube was 20 mW/cm<sup>2</sup>. The concentration of RhB was analyzed by recording the absorbance for the characteristic peak of RhB at 554 nm using the Evolution Thermo 600 UV-vis spectrophotometer. The total ROS generation activity of the few-layer g-C<sub>3</sub>N<sub>4</sub> samples was quantitatively measured by a fluorescence method based on 2',7'-dichlorofluorescein (DCFH) chromogenic agent [31,33]. The real active free radicals species were evaluated by a multiple sacrificial-agents assisted chromatometry method [34].

## 3. Results and discussion

### 3.1. Synthetic strategy

The synthetic strategy of few-layer g-C<sub>3</sub>N<sub>4</sub> is illustrated in Fig. 1. With similar structure to graphite, g-C<sub>3</sub>N<sub>4</sub> bears weak interlayer van der Waals force and intralayer covalent C–N bond (instead of C–C bond) [35]. At first, the bulk g-C<sub>3</sub>N<sub>4</sub> cluster was mixed with water, which allowed the absorbed water to be inserted into the interlayer space of g-C<sub>3</sub>N<sub>4</sub>. Then upon the sudden volume change of adsorbed water between g-C<sub>3</sub>N<sub>4</sub> layers, the g-C<sub>3</sub>N<sub>4</sub> clusters can be initially teared into few-layer nanosheets by overcoming the weak interlayer van der Waals force during the flash frozen

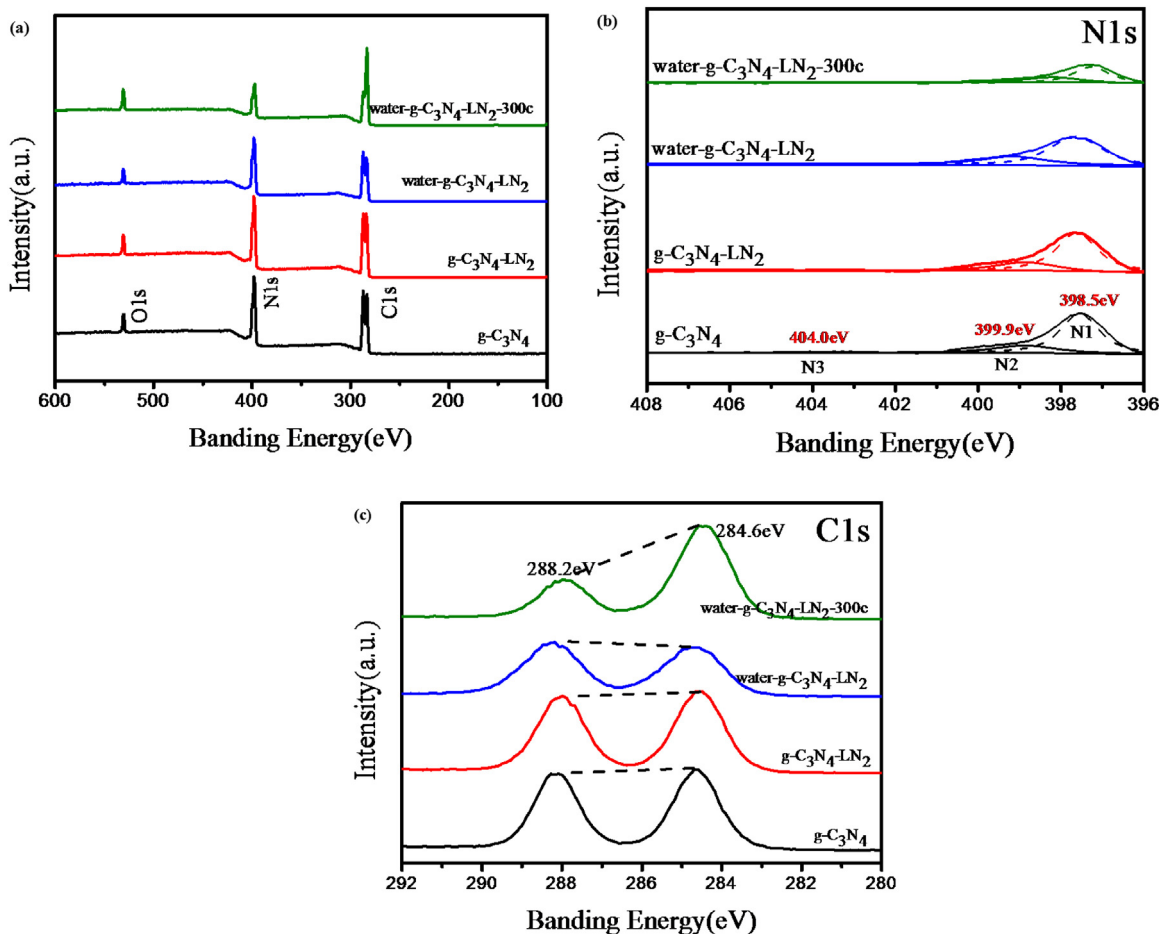


**Fig. 3.** (a) XPS survey spectra, high-resolution N1s (b) and C1s (c) of the  $\text{g-C}_3\text{N}_4$ ,  $\text{g-C}_3\text{N}_4\text{-LN}_2$ , water- $\text{g-C}_3\text{N}_4\text{-LN}_2$  and water- $\text{g-C}_3\text{N}_4\text{-LN}_2\text{-}300\text{c}$ .

process. Notably, due to the flash freezing, the immense puncturing force due to the formation of tiny ice crystals originate from interlayer adsorbed water also “etched” some C–N-containing melon units, resulting in the formation of 2D in-plane holey  $\text{g-C}_3\text{N}_4$  with size-varying holes [36]. Finally, the frozen ice can be easily removed by vacuum drying to form clean foam-like holey ultrathin few-layer  $\text{g-C}_3\text{N}_4$ . The whole process can be confirmed by the following characterizations. The main advantage of this fast proposal was waste-free and environmental-friendly, which totally eliminated thermal calcination and the use of acid/surfactant. Besides, the yield of this method was nearly 100%, which is significantly higher than conventional method, thus was attractive in scale-up production. Furthermore, this unique 2D in-plane holey structure provides more exposed edges and active sites, so the new modified few-layer  $\text{g-C}_3\text{N}_4$  is promising for environmental applications [37].

### 3.2. Crystal structure and chemical properties

The XRD patterns of pristine  $\text{g-C}_3\text{N}_4$ ,  $\text{g-C}_3\text{N}_4\text{-LN}_2$ , water- $\text{g-C}_3\text{N}_4\text{-LN}_2$  and water- $\text{g-C}_3\text{N}_4\text{-LN}_2\text{-}300\text{c}$  are presented in Fig. 2(a). These four samples all show two typical diffraction peaks around  $12.8^\circ$  and  $27.6^\circ$ , implying the basic atomic crystal structures of  $\text{g-C}_3\text{N}_4$  were largely retained during the flash deep freezing in liquid nitrogen and the subsequent calcination at  $300^\circ\text{C}$ . The peak at  $12.8^\circ$  indexed as the (100) plane corresponds to the in-plane structural packing motif of aromatic segments [38]. This distance calculated to be  $0.689\text{ nm}$  corresponds to the hole-to-hole distance in the nitride pores. Another intense peak around  $27.6^\circ$  corresponds to

the interlayer stacking of aromatic units of CN with an interlayer distance of  $0.323\text{ nm}$ , which is ascribed to the (002) plane of the stacking of the conjugated aromatic system [39]. Obviously, the exfoliation treatment gradually enhanced the (002) peak intensity of few-layer  $\text{g-C}_3\text{N}_4$ , owing to the enhanced between-layer stacking interaction of the conjugated aromatic system similar to that in graphite. Similarly, the stronger (100) plane was mostly due to an unfolded in-plane network that was associated with sufficient condensation of the conjugated framework [40]. These results indicate an improved crystallinity and thermal stability of the crystal-structured water- $\text{g-C}_3\text{N}_4\text{-LN}_2$ , which benefit the semiconductor photocatalytic activity and surface stability in aqueous solutions.

Meanwhile, the chemical structure of the samples is analyzed by Fourier transform infrared spectrometry (FTIR) (Fig. 2b). The FTIR bands reveal a typical molecular structure of  $\text{g-C}_3\text{N}_4$ . The broad peaks from  $3000$  to  $3500\text{ cm}^{-1}$  are attributed to the N–H and O–H stretching due to the free amino group and adsorbed hydroxyl species, respectively [40]. Besides the strong peaks at  $1200\text{--}1650\text{ cm}^{-1}$ , the peak at  $1640\text{ cm}^{-1}$  is attributed to C–N stretching, while the three peaks at  $1555$ ,  $1461$  and  $1405\text{ cm}^{-1}$  are contributed to the typical stretching vibrations of C–N heterocycles [41]. The peaks at  $1319$  and  $1243\text{ cm}^{-1}$  correspond to stretching vibration of connected C–NH–C units. In addition, the intense peak at  $810\text{ cm}^{-1}$  represents the characteristic breathing of triazine rings. The  $\text{g-C}_3\text{N}_4$  treated with water and liquid nitrogen reserved the typical peak at  $795\text{ cm}^{-1}$  corresponding to the breathing mode of the triazine units. While the peaks at about  $1318$  and  $1240\text{ cm}^{-1}$  become less pronounced because of electro-

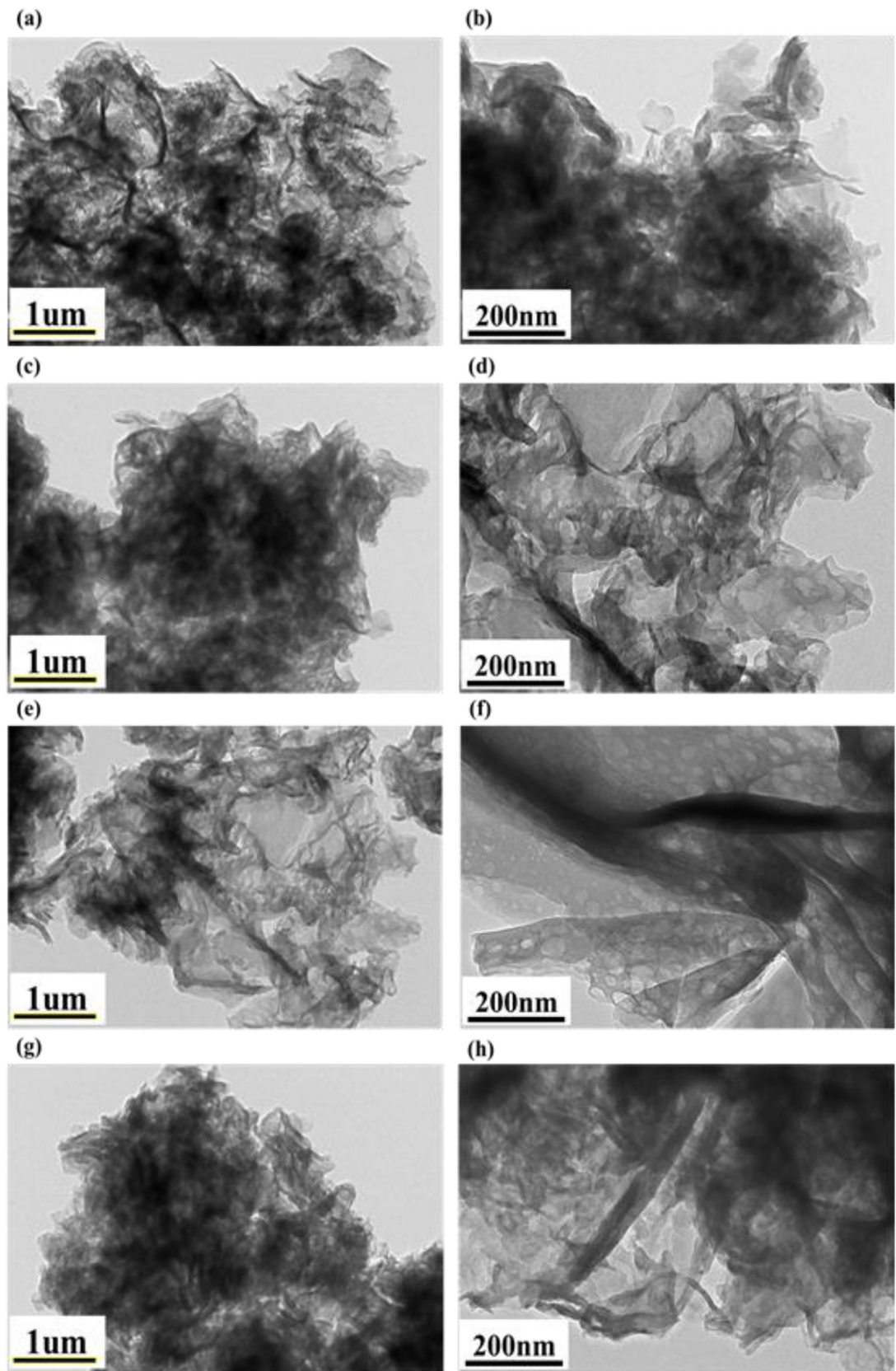


**Fig. 4.** TEM images of g-C<sub>3</sub>N<sub>4</sub> (a,b), g-C<sub>3</sub>N<sub>4</sub>-LN<sub>2</sub> (c, d), water- g-C<sub>3</sub>N<sub>4</sub>-LN<sub>2</sub> (e,f) and water-g-C<sub>3</sub>N<sub>4</sub>-LN<sub>2</sub>-300c (g,h).

static attraction between proton charge and N—(C)<sub>3</sub> groups and the decreased conjugation system of g-C<sub>3</sub>N<sub>4</sub> originating from its in-plane holes, which will be discussed below [42].

The optical adsorption properties measured by UV-vis diffuse reflectance spectroscopy are showed in Fig. 2c. It is known that the optical absorption of a semiconductor is closely related to its

electronic structure. Compared with pristine  $\text{g-C}_3\text{N}_4$ , the absorption edges of water- $\text{g-C}_3\text{N}_4\text{-LN}_2$  and water- $\text{g-C}_3\text{N}_4\text{-LN}_2\text{-}300\text{c}$  both show a remarkable blue shift. The derived band gap of water- $\text{g-C}_3\text{N}_4\text{-LN}_2$  is narrower than that of bulk  $\text{g-C}_3\text{N}_4$  (2.46 eV, 2.72 eV, Fig. 2d), which may be caused by the effect of quantum confinement effect in the nanosheet structure of water- $\text{g-C}_3\text{N}_4\text{-LN}_2$  during flash frozen exfoliation process [40]. The appropriate band edge of  $\text{g-C}_3\text{N}_4$  and the narrowed band gap of flash frozen-treated  $\text{g-C}_3\text{N}_4$  well satisfy the thermodynamic requirement for water splitting and  $\text{O}_2$  generation.

The chemical environment and surface stoichiometry of the elements were investigated via X-ray photoelectron spectroscopy (XPS). The XPS spectra reveal that all the samples are mainly composed of carbon and nitrogen, while the weak O1s peak at 532.5 eV is accredited to the small amount of adsorbed water. The C1s core XPS spectra of  $\text{g-C}_3\text{N}_4$  can be deconvoluted into two components, including the standard reference graphitic carbon (284.6 eV) and the sp<sub>2</sub>-bonded C in N=C(—N)<sub>2</sub> (288.2 eV) [43]. It should be noted that the I(graphitic C)/I(sp<sub>2</sub>-bonded C) in C1s spectra of  $\text{g-C}_3\text{N}_4$ ,  $\text{g-C}_3\text{N}_4\text{-LN}_2$  and water- $\text{g-C}_3\text{N}_4\text{-LN}_2\text{-}300\text{c}$  are all greater than 1, but is less than 1 in water- $\text{g-C}_3\text{N}_4\text{-LN}_2$ , indicating the sp<sub>2</sub>-bonded carbon species originating from the functional structure N=C(—N)<sub>2</sub> is enriched in the water- $\text{g-C}_3\text{N}_4\text{-LN}_2$ , which agrees well with XRD patterns and further supports an improved degree of crystallinity of this flash freezing exfoliated few-layer  $\text{g-C}_3\text{N}_4$  [24]. However, this unique enriched sp<sub>2</sub>-bonded carbon species structure can be destroyed by heat treatment at 300 °C as reflected by XPS. As showed on the high-resolution N1s XPS spectra (Fig. 3b), N1s could be deconvoluted into three peaks at 397.8 (N1), 398.8 (N2) and 400.5 eV (N3), demonstrating the presence of three types of N bonding. The dominant N1s signal peak at 397.8 eV could be attributed to sp<sub>2</sub> hybridized nitrogen involved in triazine rings. The peak at about 399.2 eV is commonly assigned to bridging N atoms in tertiary nitrogen (N—(C)<sub>3</sub>). The weak peak at 400.5 eV (N3) could be attributed to terminal amino functions (C—N—H). These results accord well with the FT-IR spectra. The tertiary nitrogen (N—(C)<sub>3</sub>) in water- $\text{g-C}_3\text{N}_4\text{-LN}_2$  was enriched, which well explains its high crystallinity.

### 3.3. Morphology and pore structure

The morphologies of the four samples investigated by transmission electron microscopy (TEM) are shown in Fig. 4. The bulk  $\text{g-C}_3\text{N}_4$  (Fig. 4a and b) and  $\text{g-C}_3\text{N}_4\text{-LN}_2$  (Fig. 4c and d) are irregular and thick blocks containing abundant non-uniform networks, which may be driven by the  $\pi$ - $\pi$  stacking effect between the layers and hydrogen bonding mediated by the O-containing groups [45]. However, the water- $\text{g-C}_3\text{N}_4\text{-LN}_2$  sample have an almost transparent 2D sheet-like structure (Fig. 4e and f), indicating the 2D porous  $\text{g-C}_3\text{N}_4$  layers are more flexible and largely thinner. Thus, bulk  $\text{g-C}_3\text{N}_4$  can be flash frozen exfoliated to form few-layer nanosheets. The darker part on the TEM image can be attributed to the overlap of several few-layer  $\text{C}_3\text{N}_4$  nanosheets. Notably, a large number of in-plane holes in size from several nanometers to about 50 nm are distributed in the entire flash-frozen  $\text{g-C}_3\text{N}_4$  layers. This unique ultralight foam-like structure may expose more edges in  $\text{g-C}_3\text{N}_4$ . Moreover, the resulting cross-plane diffusion channels may further improve the electron transport and charge separation efficiency [46]. After thermal treatment at 300 °C, the holey foam-like morphology of this few-layer  $\text{g-C}_3\text{N}_4$  can be nearly maintained, indicating a high thermal stability.

The nitrogen adsorption-desorption isotherms and corresponding pore size distributions curves of the series  $\text{g-C}_3\text{N}_4$  products were recorded as shown in Fig. 5. All the samples possess a typical type IV isotherm (Fig. 5) according to International Union of Pure and Applied Chemistry (IUPAC) classification, which show

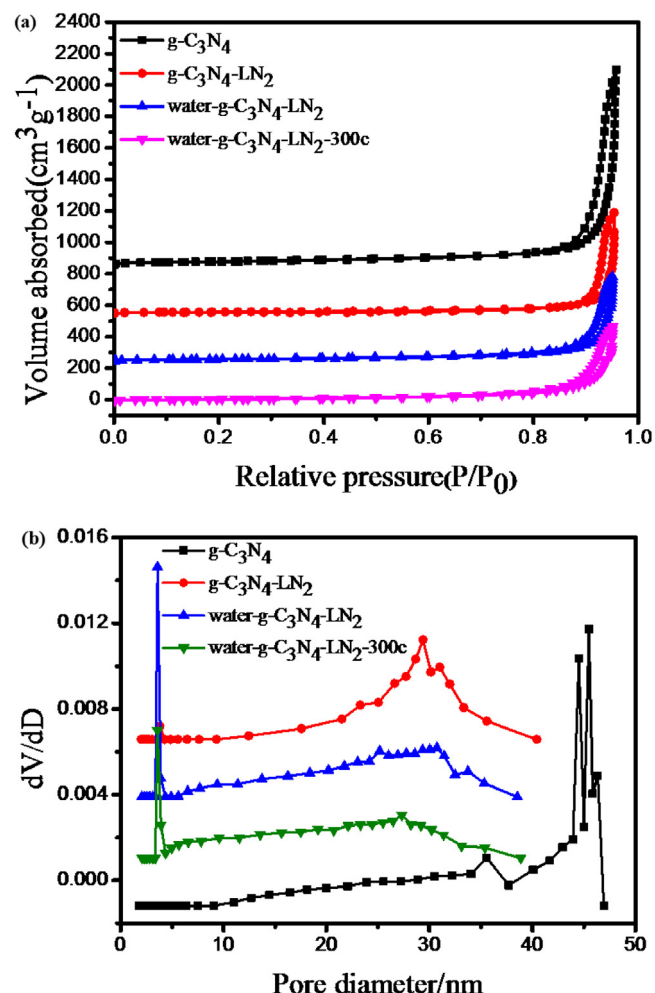


**Fig. 5.** (a) Nitrogen adsorption-desorption isotherm and (b) Barrett-Joyner-Halenda (BJH) pore size distribution of the  $\text{g-C}_3\text{N}_4$ ,  $\text{g-C}_3\text{N}_4\text{-LN}_2$ , water- $\text{g-C}_3\text{N}_4\text{-LN}_2$  and water- $\text{g-C}_3\text{N}_4\text{-LN}_2\text{-}300\text{c}$  samples.

H3 hystereses loop [47]. This indicates a mesoporous structure of both pristine  $\text{g-C}_3\text{N}_4$  and  $\text{g-C}_3\text{N}_4\text{-LN}_2$ . It is noteworthy that the hysteresis loop scope is at  $P/P_0 = 0.85\text{--}0.96$  for bare  $\text{g-C}_3\text{N}_4$ , but is narrowed down to  $P/P_0 = 0.88\text{--}0.96$  for  $\text{g-C}_3\text{N}_4\text{-LN}_2$ , indicating the small mesopores in  $\text{g-C}_3\text{N}_4$  can be destroyed by flash freezing [48]. However, the hysteresis loop scopes of the water- $\text{g-C}_3\text{N}_4\text{-LN}_2$  and water- $\text{g-C}_3\text{N}_4\text{-LN}_2\text{-}300\text{c}$  expanded to  $P/P_0 = 0.81\text{--}0.96$  and 0.82–0.96, respectively, suggesting the enrichment of small mesopores [37]. The addition of absorbed water in the surface of  $\text{g-C}_3\text{N}_4$  nanosheets validly protected the small mesopores due to the space occupying effect. This mesopore structure will benefit the molecular diffusion and mass transfer in photocatalytic applications. As showed in Fig. 5, the water- $\text{g-C}_3\text{N}_4\text{-LN}_2$  has the most abundant pore size distribution. The calculated Brunauer-Emmett-Teller (BET) surface areas and pore volume of all samples are listed in Table 1. Clearly, the water- $\text{g-C}_3\text{N}_4\text{-LN}_2$  has larger specific surface area compared with bulk  $\text{g-C}_3\text{N}_4$  (135.6 vs. 108.6 m<sup>2</sup>/g). After flash freezing treatment without the protection of surface absorbed water, the specific surface area of  $\text{g-C}_3\text{N}_4\text{-LN}_2$  decreased to 78.3 m<sup>2</sup>/g. The specific surface area of water- $\text{g-C}_3\text{N}_4\text{-LN}_2\text{-}300\text{c}$  also decreased to 70.8 m<sup>2</sup>/g because of heating induced pore structure degradation, however, the presence of small mesopores can still promise a fast molecular diffusion in photocatalytic process. Overall, the pore structure and surface property of  $\text{g-C}_3\text{N}_4$  were optimized after flash frozen treatment with the presence of surface absorbed water. The high specific surface area and porous structure of water- $\text{g-C}_3\text{N}_4\text{-LN}_2$

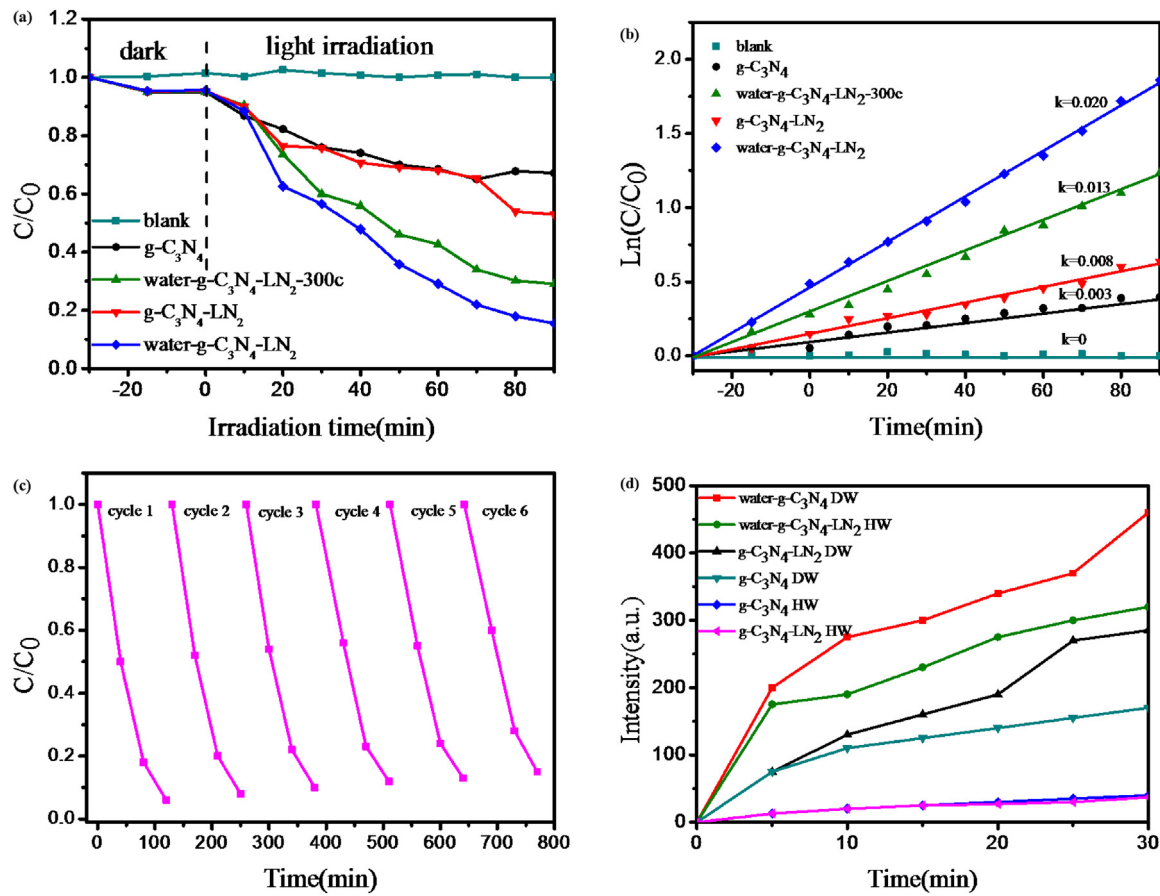


**Fig. 6.** (a) Photocatalytic curves on degradation of RhB dye under solar light irradiation over different photocatalysts and (b) corresponding kinetic curves of g-C<sub>3</sub>N<sub>4</sub>, g-C<sub>3</sub>N<sub>4</sub>-LN<sub>2</sub>, water-g-C<sub>3</sub>N<sub>4</sub>-LN<sub>2</sub> and water-g-C<sub>3</sub>N<sub>4</sub>-LN<sub>2</sub>-300c samples (c) Photocatalytic time course of water-g-C<sub>3</sub>N<sub>4</sub>-LN<sub>2</sub> sample under visible light irradiation (d) ROS generation curves of g-C<sub>3</sub>N<sub>4</sub>-LN<sub>2</sub>, water-g-C<sub>3</sub>N<sub>4</sub>-LN<sub>2</sub> and bare g-C<sub>3</sub>N<sub>4</sub> in both normoxic deionized water (DW) and hypoxic water (HW).

**Table 1**

Physicochemical properties of the g-C<sub>3</sub>N<sub>4</sub>, g-C<sub>3</sub>N<sub>4</sub>-LN<sub>2</sub>, water-g-C<sub>3</sub>N<sub>4</sub>-LN<sub>2</sub> and water-g-C<sub>3</sub>N<sub>4</sub>-LN<sub>2</sub>-300c samples.

Sample	Specific surface area(m <sup>2</sup> /g)	Pore volume(cm <sup>3</sup> /g)	Eg(eV)	I(graphitic C)/I(sp2C)
g-C <sub>3</sub> N <sub>4</sub>	108.6	0.94	2.72	1.12
g-C <sub>3</sub> N <sub>4</sub> -LN <sub>2</sub>	78.3	0.79	2.69	1.16
water-g-C <sub>3</sub> N <sub>4</sub> -LN <sub>2</sub>	135.6	1.14	2.46	0.76
water-g-C <sub>3</sub> N <sub>4</sub> -LN <sub>2</sub> -300c	70.8	0.84	2.41	2.54

LN<sub>2</sub> effectively promote the photocatalytic reaction by increasing the density of active sites and facilitating mass transfer [49].

#### 3.4. Photocatalytic performance

Fig. 6a shows the RhB photodegradation efficiency as a function of irradiation time under visible light irradiation, where C<sub>0</sub> and C are the RhB concentrations after adsorption-desorption equilibration and after certain period of irradiation, respectively. No obvious photodegradation is detected in the blank experiment (no photocatalyst), which verified the stability of RhB in this test condition [50]. Except for the slight adsorption in dark time, the photocatalytic efficiency of pure g-C<sub>3</sub>N<sub>4</sub> and after 100 min of visible light irradiation is only 30%. Remarkably, the RhB photocatalytic degradation over water-g-C<sub>3</sub>N<sub>4</sub>-LN<sub>2</sub> is efficient and nearly 80% of the dye is completely removed after 80 min of irradiation. The water-g-C<sub>3</sub>N<sub>4</sub>-LN<sub>2</sub>-300c show only a little decreased photocatalytic degradation rate of RhB, indicating the excellent thermal stability of water-g-C<sub>3</sub>N<sub>4</sub>-LN<sub>2</sub>. The kinetic curves of RhB degradation can be approximated as a pseudo-first-order process by linear transform  $\ln(C_0/C) = kt$  [51] (Fig. 6c). Under the same experimen-

tal conditions, the pseudo-first order reaction kinetics (*k*) of RhB degradation over the water-g-C<sub>3</sub>N<sub>4</sub>-LN<sub>2</sub> is 0.20, which is much higher than that of water-g-C<sub>3</sub>N<sub>4</sub>-LN<sub>2</sub>-300c (*k* = 0.13), g-C<sub>3</sub>N<sub>4</sub>-LN<sub>2</sub> (*k* = 0.08) and bulk g-C<sub>3</sub>N<sub>4</sub> (*k* = 0.03), respectively. The results above indicate that water-g-C<sub>3</sub>N<sub>4</sub>-LN<sub>2</sub> should be an excellent photocatalytic system for enhanced photocatalytic activity compared with common bulk g-C<sub>3</sub>N<sub>4</sub>. Furthermore, as shown in Fig. 6d, the photocatalytic activity after 6 successive cycles only slightly decreased, indicating it is fairly stable under the studied conditions.

The ROS generation ability in both normoxic deionized water and hypoxic water was measured by using 2',7'-dichlorofluorescein (DCFH), an ROS fluorescence sensor. The ROS generation amounts of g-C<sub>3</sub>N<sub>4</sub>-LN<sub>2</sub>, water-g-C<sub>3</sub>N<sub>4</sub>-LN<sub>2</sub> and bare g-C<sub>3</sub>N<sub>4</sub> sample are shown in Fig. 6c, it can be found the ROS generation ability of water-g-C<sub>3</sub>N<sub>4</sub>-LN<sub>2</sub> in normoxic water was of little significant compared with bare g-C<sub>3</sub>N<sub>4</sub> with in 30 min. However, in the hypoxic environment, after 15 min of laser irradiation, the ROS productions by g-C<sub>3</sub>N<sub>4</sub>-LN<sub>2</sub> and g-C<sub>3</sub>N<sub>4</sub> were extremely weak. Interestingly, remarkable fluorescence of DCFH was detected in water-g-C<sub>3</sub>N<sub>4</sub>-LN<sub>2</sub> in hypoxic water, verifying that the ROS generation ability was unaffected under light irradiation [23]. This result indicates that

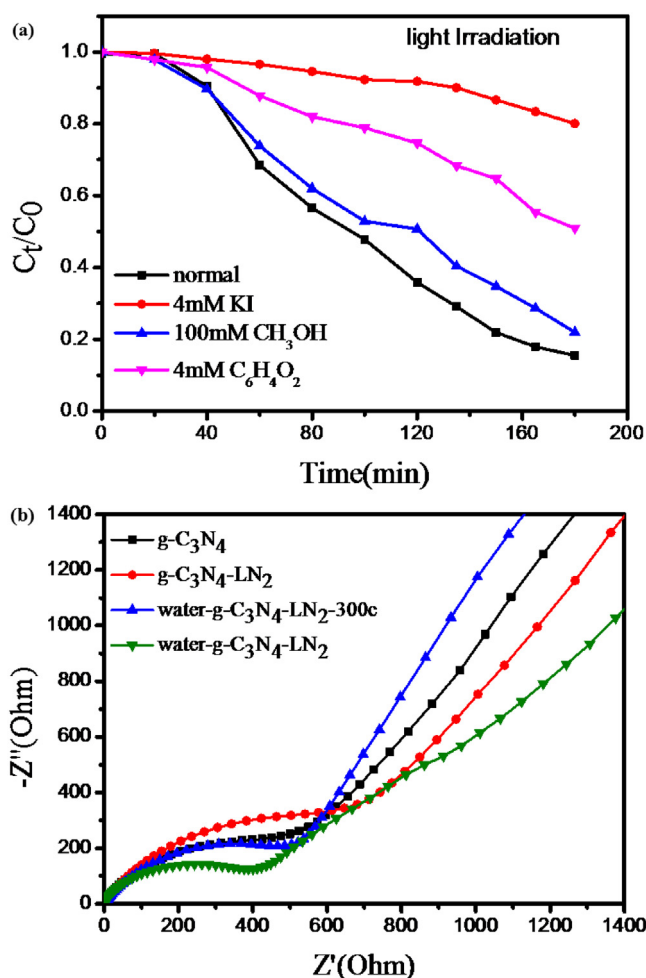
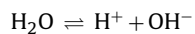


**Fig. 7.** (a) Plots of photogenerated carriers trapped during the photocatalytic degradation of RhB and (b) EIS of the different photocatalysts in a 0.1 M NaNO<sub>3</sub> aqueous solution.

water-\$g\$-\$\text{C}\_3\text{N}\_4\$-\$\text{LN}\_2\$ may overcome the hypoxia restricts in solution and thereby improve the photocatalytic efficacy in hypoxia environmental and biological applications.

### 3.5. ROS generation mechanism

To investigate and identify the main ROS species generated in the visible-light-driven photocatalytic process responsible for the degradation of pollutants, experiments were performed in the presence of KI (a scavenger for h<sup>+</sup> and •OH radicals on the catalyst surface), methanol (CH<sub>3</sub>OH, a scavenger for •OH radicals in the solution), and 1,4-benzoquinone (C<sub>6</sub>H<sub>4</sub>O<sub>2</sub>, a scavenger for O<sup>•2-</sup>) respectively [52]. The results shown in Fig. 7a indicate that the degradation efficiencies of RhB significantly decreased from 80.0% to 20.3% after 180 min in the presence of 4 mM KI. When 4 mM C<sub>6</sub>H<sub>4</sub>O<sub>2</sub> was added to the reaction system, the degradation efficiency of RhB slightly decreased to 50.5%. However, 100 mM CH<sub>3</sub>OH just affect the degradation efficiency a little. These results indicated that h<sup>+</sup> on the catalyst surface is the most important oxidising species during the photocatalytic process, that O<sup>•2-</sup> is also responsible for the degradation of RhB, and that •OH in the solution is not the main active species. The reaction equations in the photocatalytic process were proposed (Eqs. (1)–(7)) based on the experimental results.



The electrical conductivity and photogenerated charge separation were investigated via electrochemical impedance spectroscopy (EIS). The EIS Nyquist plots of \$g\$-\$\text{C}\_3\text{N}\_4\$, \$g\$-\$\text{C}\_3\text{N}\_4\$-\$\text{LN}\_2\$, water-\$g\$-\$\text{C}\_3\text{N}\_4\$-\$\text{LN}\_2\$ and water-\$g\$-\$\text{C}\_3\text{N}\_4\$-\$\text{LN}\_2\$-300c electrodes under visible light irradiation are shown in Fig. 7b. The arc radius on EIS Nyquist plot of water-\$g\$-\$\text{C}\_3\text{N}\_4\$-\$\text{LN}\_2\$ heterojunction is smaller than other samples. As reported, a smaller arc radius of the EIS Nyquist plot suggests a more effective separation of photogenerated electron-hole pairs and the faster interfacial charge transfer. These results suggest water-\$g\$-\$\text{C}\_3\text{N}\_4\$-\$\text{LN}\_2\$ has dramatically smaller charge transfer resistance and higher electron-hole separation/transfer efficiency. The enhanced photoelectric properties can be attributed to the large number of in-plane holes that greatly facilitates the mass transfer and improves photogenerated charge mobility.

In summary, the drastic enhancement of photocatalytic activity for water-\$g\$-\$\text{C}\_3\text{N}\_4\$-\$\text{LN}\_2\$ can be explained below. First, the high crystallinity of water-\$g\$-\$\text{C}\_3\text{N}\_4\$-\$\text{LN}\_2\$, which resulted from the sudden layer-stacked stamping by frozen water during flash freezing, may greatly improve the visible light harvest and surface stability in aqueous solutions. Second, the holey 2D ultrathin structure of \$g\$-\$\text{C}\_3\text{N}\_4\$ nanosheets provides large specific surface areas, more exposed new edges, and more catalytic active sites [21]. Third, this unique structure improves the electron transport ability, and the in-plane holes in water-\$g\$-\$\text{C}\_3\text{N}\_4\$-\$\text{LN}\_2\$ also accelerate the cross-plane diffusion of photogenerated carriers.

## 4. Conclusions

Foam-like holey few-layer \$g\$-\$\text{C}\_3\text{N}\_4\$ nanosheets was successfully prepared by a simple cost-effective method through the fast flash freezing exfoliation of bulk \$g\$-\$\text{C}\_3\text{N}\_4\$ with the assistance of absorbed water. The as-prepared 2D holey few-layer \$g\$-\$\text{C}\_3\text{N}\_4\$ performed well in ROS generation and dye photodegradation under visible light. The remarkable ROS generation ability of the few-layer \$g\$-\$\text{C}\_3\text{N}\_4\$ can be attributed to the high visible light harvest, more exposed edges, more catalytic active sites and fast electron transportation. Our findings represent significant progress in scalable high-yield fabrication of ultrathin \$g\$-\$\text{C}\_3\text{N}\_4\$. This novel strategy is effective for the generation of tailored \$g\$-\$\text{C}\_3\text{N}\_4\$ nanostructures that improve the photocatalytic activity and applicability.

## Acknowledgements

This work was supported by National Natural Science Foundation of China (Grant No. 51528202, 51671136 and 51502172), "Shu Guang" project (Grant No. 13SG46) supported by Shanghai Municipal Education Commission and Shanghai Education Development Foundation and Capacity-Building of Local University Project by Science and Technology Commission of Shanghai Municipality (Grant No. 12160502400).

## References

- [1] K. Singh, J. Nowotny, V. Thangadurai, Chem. Soc. Rev. 42 (2013) 1961–1972.
- [2] D.E.J.G.J. Dolmans, D. Fukumura, R.K. Jain, Nat. Rev. Cancer 3 (2003) 380–387.
- [3] C.C. Chen, W.H. Ma, J.C. Zhao, Chem. Soc. Rev. 39 (2010) 4206–4219.

[4] M. Kapilashrami, Y.F. Zhang, Y.S. Liu, A. Hagfeldt, J.H. Guo, *Chem. Rev.* 114 (2014) 9662–9707.

[5] Y. Hu, X.H. Gao, L. Yu, Y.R. Wang, J.Q. Ning, S.J. Xu, X.W. Lou, *Angew. Chem. Int. Ed.* 52 (2013) 5636–5639.

[6] J. Di, J.X. Xia, X.W. Li, M.X. Ji, H. Xu, Z.G. Chen, H.M. Li, *Carbon* 107 (2016) 1–10.

[7] X.R. Du, G.J. Zou, Z.H. Wang, X.L. Wang, *Nanoscale* 7 (2015) 8701–8706.

[8] W. Fu, H.Y. He, Z.H. Zhang, C.Y. Wu, X.W. Wang, H. Wang, Q.S. Zeng, L.F. Sun, X.L. Wang, J.D. Zhou, Q.D. Fu, P. Yu, Z.X. Shen, C.H. Jin, B.I. Yakobson, Z. Liu, *Nano Energy* 27 (2016) 44–50.

[9] S.W. Hu, L.W. Yang, Y. Tian, X.L. Wei, J.W. Ding, J.X. Zhong, P.K. Chu, *J. Colloid Interface Sci.* 431 (2014) 42–49.

[10] D.D. Zheng, X.N. Cao, X.C. Wang, *Angew. Chem. Int. Ed.* 55 (2016) 11512–11516.

[11] W.J. Ong, L.L. Tan, Y.H. Ng, S.T. Yong, S.P. Chai, *Chem. Rev.* 116 (2016) 7159–7329.

[12] Q. Han, B. Wang, J. Gao, Z.H. Cheng, Y. Zhao, Z.P. Zhang, L.T. Qu, *ACS Nano* 10 (2016) 2745–2751.

[13] Y.T. Gong, M.M. Li, H.R. Li, Y. Wang, *Green Chem.* 17 (2015) 715–736.

[14] Z.J. Huang, F.B. Li, B.F. Chen, G.Q. Yuan, *ChemSusChem* 9 (2016) 478–484.

[15] Y.L. Liao, S.M. Zhu, J. Ma, Z.H. Sun, C. Yin, C.L. Zhu, X.H. Lou, D. Zhang, *ChemCatChem* 6 (2014) 3419–3425.

[16] Z. Yang, Y.J. Zhang, Z. Schnepp, *J. Mater. Chem. A* 3 (2015) 14081–14092.

[17] G.H. Dong, K. Zhao, L.Z. Zhang, *Chem. Commun.* 48 (2012) 6178–6180.

[18] L.Q. Zhang, X. He, X.W. Xu, C. Liu, Y.L. Duan, L.Q. Hou, Q.D. Zhou, C. Ma, X.P. Yang, R. Liu, F. Yang, L.S. Cui, C.M. Xu, Y.F. Li, *Appl. Catal. B-Environ.* 203 (2017) 1–8.

[19] H.H. Liu, D.L. Chen, Z.Q. Wang, H.J. Jing, R. Zhang, *Appl. Catal. B-Environ.* 203 (2017) 300–313.

[20] S. Bai, X.J. Wang, C.Y. Hu, M.L. Xie, J. Jiang, Y.J. Xiong, *Chem. Commun.* 50 (2014) 6094–6097.

[21] H.X. Zhao, H.T. Yu, X. Quan, S. Chen, H.M. Zhao, H. Wang, *RSC Adv.* 4 (2014) 624–628.

[22] J.Z. Jiang, O.Y. Lei, L.H. Zhu, A.M. Zheng, J. Zou, X.F. Yi, H.Q. Tang, *Carbon* 80 (2014) 213–221.

[23] E.G. Ju, K. Dong, Z.W. Chen, Z. Liu, C.Q. Liu, Y.Y. Huang, Z.Z. Wang, F. Pu, J.S. Ren, X.G. Qu, *Angew. Chem. Int. Ed.* 55 (2016) 11467–11471.

[24] Y.F. Li, R.X. Jin, Y. Xing, J.Q. Li, S.Y. Song, X.C. Liu, M. Li, R.C. Jin, *Adv. Energy Mater.* 24 (2016), <http://dx.doi.org/10.1002/aenm.201601273>.

[25] Y.G. Wang, X. Bai, H.F. Qin, F. Wang, Y.G. Li, X. Li, S.F. Kang, Y.H. Zuo, L.F. Cui, *ACS Appl. Mater. Interfaces* 8 (2016) 17212–17219.

[26] P. Niu, L.L. Zhang, G. Liu, H.M. Cheng, *Adv. Funct. Mater.* 22 (2012) 4763–4770.

[27] S.B. Yang, Y.J. Gong, J.S. Zhang, L. Zhan, L.L. Ma, Z.Y. Fang, R. Vajtai, X.C. Wang, P.M. Ajayan, *Adv. Mater.* 25 (2013) 2452–2456.

[28] X.P. Dong, F.X. Cheng, *J. Mater. Chem. A* 3 (2015) 23642–23652.

[29] J. Xu, L.W. Zhang, R. Shi, Y.F. Zhu, *J. Mater. Chem. A* 1 (2013) 14766–14772.

[30] W. Bing, Z.W. Chen, H.J. Sun, P. Shi, N. Gao, J.S. Ren, X.G. Qu, *Nano Res.* 8 (2015) 1648–1658.

[31] D.W. Zheng, B. Li, C.X. Li, J.X. Fan, Q. Lei, C. Li, Z.S. Xu, X.Z. Zhang, *ACS Nano* 10 (2016) 8715–8722.

[32] Y.W. Zhang, J.H. Liu, G. Wu, W. Chen, *Nanoscale* 4 (2012) 5300–5303.

[33] Y.Y. Yuan, J. Liu, B. Liu, *Angew. Chem. Int. Ed.* 53 (2014) 7163–7168.

[34] F.T. Li, Y. Zhao, Y.J. Hao, X.J. Wang, R.H. Liu, D.S. Zhao, D.M. Chen, *J. Hazard. Mater.* 239 (2012) 118–127.

[35] Q. Liu, T.X. Chen, Y.R. Guo, Z.G. Zhang, X.M. Fang, *Appl. Catal. B-Environ.* 193 (2016) 248–258.

[36] T.T. Yu, L.F. Liu, L. Li, F.L. Yang, *Electrochim. Acta* 210 (2016) 122–129.

[37] X.J. She, L. Liu, H.Y. Ji, Z. Mo, Y.P. Li, L.Y. Huang, D.L. Du, H. Xu, H.M. Li, *Appl. Catal. B-Environ.* 187 (2016) 144–153.

[38] S.W. Hu, L.W. Yang, Y. Tian, X.L. Wei, J.W. Ding, J.X. Zhong, P.K. Chu, *Appl. Catal. B-Environ.* 163 (2015) 611–622.

[39] K. Kalasam, J.D. Epping, A. Thomas, S. Losse, H. Junge, *Energy Environ. Sci.* 4 (2011) 4668–4674.

[40] Q.H. Liang, Li Zhi, Z.H. Huang, Feiyu Kang, Q.H. Yang, *Adv. Funct. Mater.* 25 (2015) 6885–6892.

[41] L. Zhang, M.N. Ou, H.C. Yao, Z.H. Li, D.Y. Qu, F. Liu, J.C. Wang, J.S. Wang, Z.J. Li, *Electrochim. Acta* 186 (2015) 292–301.

[42] J.L. Zhang, Z.W. Zhu, J.W. Di, Y.M. Long, W.F. Li, Y.F. Tu, *Electrochim. Acta* 186 (2015) 192–200.

[43] J.H. Sun, J.S. Zhang, M.W. Zhang, M. Antonietti, X.Z. Fu, X.C. Wang, *Nat. Commun.* 3 (2012).

[45] J.G. Yu, S.H. Wang, J.X. Low, W. Xiao, *Phys. Chem. Chem. Phys.* 15 (2013) 16883–16890.

[46] J.Q. Yan, H. Wu, H. Chen, Y.X. Zhang, F.X. Zhang, S.F. Liu, *Appl. Catal. B-Environ.* 191 (2016) 130–137.

[47] X.Y. Yuan, C. Zhou, Y.R. Jin, Q.Y. Jing, Y.L. Yang, X. Shen, Q. Tang, Y.H. Mu, A.K. Du, *J. Colloid Interface Sci.* 468 (2016) 211–219.

[48] J.X. Xia, M.X. Ji, J. Di, B. Wang, S. Yin, Q. Zhang, M.Q. He, H.M. Li, *Appl. Catal. B-Environ.* 191 (2016) 235–245.

[49] W. Chen, T. Huang, Y.X. Hua, T.Y. Liu, X.H. Liu, S.M. Chen, *J. Hazard. Mater.* 320 (2016) 529–538.

[50] W. Zhao, Y. Guo, S.M. Wang, H. He, C. Sun, S.G. Yang, *Appl. Catal. B-Environ.* 165 (2015) 335–343.

[51] W. Chen, T.Y. Liu, T. Huang, X.H. Liu, J.W. Zhu, G.R. Duan, X.J. Yang, *Appl. Surf. Sci.* 355 (2015) 379–387.

[52] X.Q. Zhu, J.L. Zhang, F. Chen, *Appl. Catal. B-Environ.* 102 (2011) 316–322.